### Effect of demagnetization factors on spin current transport

Po-Hsun Wu, 1,\* Ying-Ting Chan, 2,\* Tzu-Chao Hung, 2 Yi-Hui Zhang, 1,2 Danru Qu (0,2,† Tien-Ming Chuang, 2,‡ C. L. Chien, 1,3 and Ssu-Yen Huang, 1,8 <sup>1</sup>Department of Physics, National Taiwan University, Taipei 16017, Taiwan <sup>2</sup>Institute of Physics, Academia Sinica, Taipei 11529, Taiwan <sup>3</sup>Department of Physics and Astronomy, Johns Hopkins University, Baltimore, Maryland 21218, USA

(Received 19 August 2020; revised 23 October 2020; accepted 30 October 2020; published 16 November 2020)

The demagnetizing field associated with shape anisotropy originates from the magnetic field generated through magnetization of magnetic materials. The shape and demagnetizing effects must be considered as characteristics of a magnetic object in the presence of a magnetic field. In this study, we demonstrated the strong influence of the demagnetizing field on the spin current transports in Pt/YIG, including the spin Seebeck effect, spin Hall effect, spin Hall magnetoresistance, and planar Hall resistance. The calculated effective demagnetizing factors were closely related to the thickness- and width-dependent anomalous plateau behaviors of the spin-dependent electrical and thermal transports as well as magneto-optical measurements. Moreover, we demonstrated that the width of the plateau manifested from the shape of the YIG sample. Furthermore, through magnetic force microscopy, we directly visualized the evolution of the magnetic domains with an abrupt 90° magnetic rotation, which we further corroborated by the 90° resistance phase shift in the angular-dependent planar Hall effect.

DOI: 10.1103/PhysRevB.102.174426

#### I. INTRODUCTION

Pure spin current is a significant phenomenon in the field of spintronics, with promising applications in energy-efficient data storage and energy harvesting. The generation and detection of pure spin current with efficient transport of spin angular momentum have been experimentally demonstrated through the spin Hall effect (SHE) [1], spin pumping [2,3], spin Hall magnetoresistance [4–6], nonlocal transport [2,7], and spin Seebeck effect (SSE) [8–11]. Notably, many of the aforementioned spin current phenomena were first reported not in thin films but in bulk specimens. The specimen shape and the associated demagnetizing field  $H_d$ , which tends to reduce the total magnetization of the specimen, can have major effects on the spin current phenomenon. However, the demagnetizing field  $H_d$  can only be analytically calculated when the internal magnetic field is uniform for certain geometrical shapes such as ellipsoids. The sample shape and the demagnetizing field should have considerable effects on spin current, especially in bulk ferrimagnetic [2-5,8-10] and antiferromagnetic [6,7,11–13] insulators.

The ferrimagnetic insulator yttrium iron garnet (YIG) is one of the most commonly used materials in insulator-based spintronics and spin caloritronics [14-16]. YIG has been extensively used in the demonstration of the pure spin current phenomenon because it has a substantial Curie temperature of 550 K and exceptionally low magnetic damping, with no

potential artifacts from charge current. The most common shape of bulk YIG used to explore the pure spin current phenomenon is a slab. In this study, we demonstrated how the pure spin current, demagnetization factor, and shape of the YIG slab are associated. We also demonstrated that the shape anisotropy of the YIG specimen significantly influences the spin-dependent electrical and thermal transports as well as the magneto-optical measurements in YIG-based heterostructures. We used the theoretical model and numerical calculations to quantitatively describe the thicknessand width-dependent spin current transport by considering the effective demagnetization factors. Furthermore, the paper presents visual images of the evolution of the magnetic domains to reveal an abrupt magnetic domain flop phenomenon, which was further corroborated by the 90° resistance phase shift in the angular-dependent planar Hall effect (PHE).

#### II. EXPERIMENT

To investigate the effect of demagnetization factors, we used high-quality single-crystalline (111) and polycrystalline rectangular YIG slabs. To obtain slabs of varied sizes, we systematically changed the thickness from 1 mm to 20  $\mu$ m and the specimen width from 30 to 1 mm. A 5-nm-thick Pt film deposited on the YIG through magnetron sputtering was used to generate or detect the pure spin current through the spin Hall effect (SHE) or inverse spin Hall effect (ISHE), respectively. The thin Pt films were patterned into the Hall bar structure through photolithography with a linewidth of 10  $\mu$ m for electrical and thermal transport measurements [17,18]. For the spin Hall magnetoresistance (SMR) and PHE measurements, we generated a pure spin current through SHE by using electric current. For the ISHE measurement, we

<sup>\*</sup>These authors contributed equally to this work.

<sup>†</sup>danru@gate.sinica.edu.tw

<sup>‡</sup>chuangtm@gate.sinica.edu.tw

<sup>§</sup>syhuang@phys.ntu.edu.tw

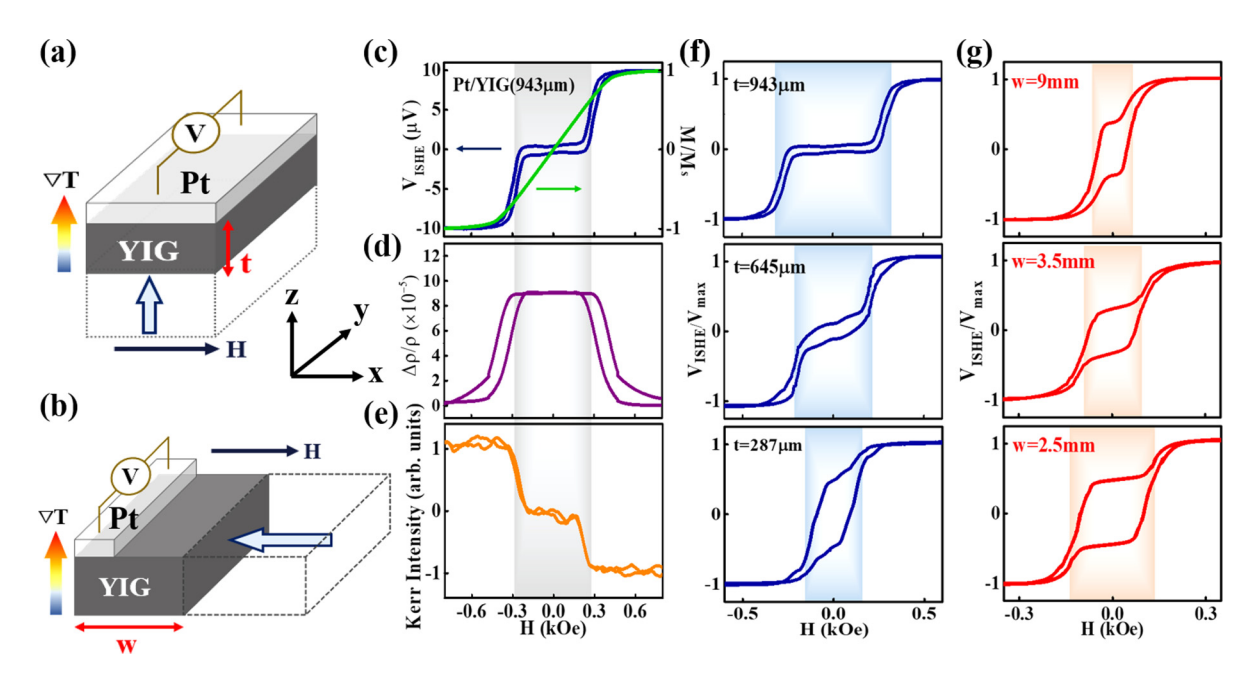


FIG. 1. Schematic diagram for (a) the thickness dependent and (b) the width dependent measurement geometry. The blue arrows indicate the grinding process to reduce (a) the thickness t and (b) the width w to keep the same interface between Pt and YIG.  $\nabla T$  and H denote the temperature gradient and the external magnetic field. (c) The ISHE of Pt on single crystal YIG (blue) and the normalized M-H loop of YIG (green). (d) The SMR of Pt/YIG. (e) Normalized Kerr intensity of YIG slab. The ISHE of Pt/YIG with different (f) thickness of YIG and (g) width of YIG. The shaded areas in (c)–(g) represent the plateau width.

generated a pure magnonic spin current in YIG through SSE by using a thermal gradient. We investigated the configuration of the surface magnetization by measuring the magneto-optic Kerr effect (MOKE) with a diode laser with a wavelength of 408 nm. Magnetic domain images were obtained through field-dependent magnetic force microscopy (MFM).

For consistency in the study of the thickness dependence of the YIG slab, we used only one YIG slab with the same 5-nm Pt top layer and interface through systematic reduction of the YIG thickness, which was achieved by grinding the back side of the slab, as shown in Fig. 1(a). Similarly, to study the width dependence of the slab, we used only one slab sample with the Pt film deposited on one side and systematically reduced the width by grinding the opposite side, as shown in Fig. 1(b). Thus, the SSE, SMR, and MOKE measurements were performed on the identical surfaces of YIG but with thickness or width varied.

#### III. RESULTS AND DISCUSSION

The experimental schematics of the SSE and ISHE in the Pt/YIG are shown in Figs. 1(a) and 1(b). The SSE with a thermal gradient applied in the z direction injects a spin current from the YIG into the Pt layer, with the spin index in the x direction aligned by the external magnetic field. The ISHE in the Pt layer generates an electrical field,  $E_{\rm ISHE} \propto j_s \times \sigma$ , where  $j_s$  is the spin current density and  $\sigma$  is the spin orientation of the spin current set by the net magnetization of the YIG, which is detected as voltage  $V_{\rm ISHE}$  in the y direction. The results are shown in Fig. 1(c) (blue curve). The field dependence of magnetization (M), as measured by a magnetometer [Fig. 1(c) (green curve)], varies smoothly from negative to positive M values. The field dependence of  $V_{\rm ISHE}$  is distinctly different

and yields a plateau between -0.3 and +0.3 kOe. This plateau behavior has been observed in numerous SSE studies that have used bulk YIG [3–5,8–10]. A similar plateau behavior was also observed for the field dependence of SMR and MOKE, as shown in Figs. 1(d) and 1(e), respectively. Previously, we suggested that this anomalous plateau was formed as a result of the noncollinear magnetization at the YIG surface [19]. In this study, we demonstrated that the plateau behavior resulted from the effective demagnetization of the YIG slab with low magnetic anisotropy.

When the thickness (t) of the YIG slab was systematically reduced from 943  $\mu$ m, the width of the field plateau systematically decreased, as shown by the three representative results in Fig. 1(f). In another set of experiments, we systematically reduced the width (w) of the specimen before taking measurements. As shown in Fig. 1(g), reducing w results in an increase in the width of the field plateau. The distinct behaviors at varying thicknesses (t) and widths (w) are shown in Figs. 2(a) and 2(b), respectively. Notably, SMR and MOKE

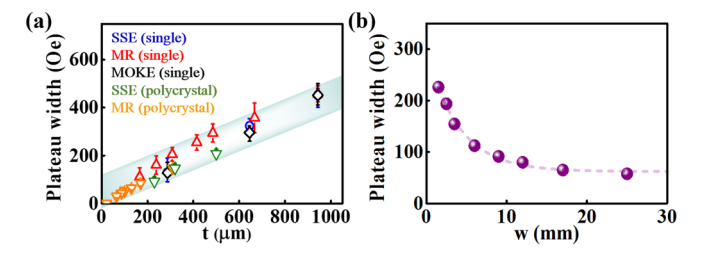


FIG. 2. The field width plateau as a function of (a) YIG thickness from the SSE, SMR, and MOKE measurements by using both single-crystalline and polycrystalline YIG slabs with a width of 3 mm and (b) YIG width from the SSE measurement.

exhibited the same magnetic field dependence and the same plateau width as those of SSE, as shown in Figs. 1(c)-1(e). Figure 2(a) presents the results obtained from the SSE, SMR, and MOKE measurements by using both single-crystalline and polycrystalline YIG slabs with a width of 3 mm. These results clearly demonstrate the thickness dependence of the plateau, which increased quasilinearly with the thickness, with little or no difference between single-crystalline and polycrystalline specimens. By contrast, when the width (w) of the polycrystalline YIG slab was altered, the plateau width decreased quasiexponentially with increasing w and reached a terminal value at w > 15 mm at a fixed thickness of  $500 \ \mu m$ , as shown in Fig. 2(b). These geometry-dependent results suggest a common physical origin—the demagnetization factor of the YIG slabs.

To investigate the effect of the demagnetization factor, we studied the magnetic anisotropy of YIG. The total effective anisotropy energy  $K_{\rm eff}$  is the area difference of the hysteresis loops between the in-plane field  $H_{\perp}$ , expressed as follows [20,21]:

$$K_{\text{eff}} = \int H_{\parallel} dM_{\parallel} - \int H_{\perp} dM_{\perp}. \tag{1}$$

The in-plane saturation field increases, whereas the out-ofplane saturation field decreases with increasing YIG thickness (t), as shown in Figs. 3(a) and 3(b), respectively. Consequently, when the magnetic moments are compelled to lie in plane for a small thickness t, they have the propensity to tilt out of the plane in a thicker YIG slab. The total effective anisotropy energy per unit area given by  $(K_{\text{eff}})t$  [blue circles in Fig. 3(c)] includes the magnetocrystalline anisotropy  $K_{\text{cry}}$ , strain anisotropy  $K_{\text{me}}$ , shape anisotropy  $K_{\text{h}}$ , and surface anisotropy  $K_{\text{s}}$  [20,22]:

$$(K_{\rm eff})t = (K_{\rm cry} + K_{\rm me} + K_{\rm h})t + 2K_s.$$
 (2)

As shown in Fig. 3(c),  $(K_{\rm eff})t$  decreases with decreasing YIG thickness (t). Here, the value of  $K_{\rm cry}$  for a single-crystal bulk YIG is  $5.7 \times 10^3$  erg/cm<sup>3</sup> [22,23];  $K_{\rm s}$  and  $K_{\rm me}$  can be neglected because YIG is in the slab form with a thickness of a few micrometers to millimeters.

Next, we evaluate the role of  $K_h$ , which is dependent on the geometrical shape of the sample associated with the magnetostatic energy. It can be expressed in a quadratic form with the magnetization components as follows:

$$K_{\rm h} = \frac{1}{2}(N_w - N_t)M^2,$$
 (3)

where  $N_w$  and  $N_t$  are the diagonal elements of demagnetizing factors tensor along the width and thickness of the YIG slab,

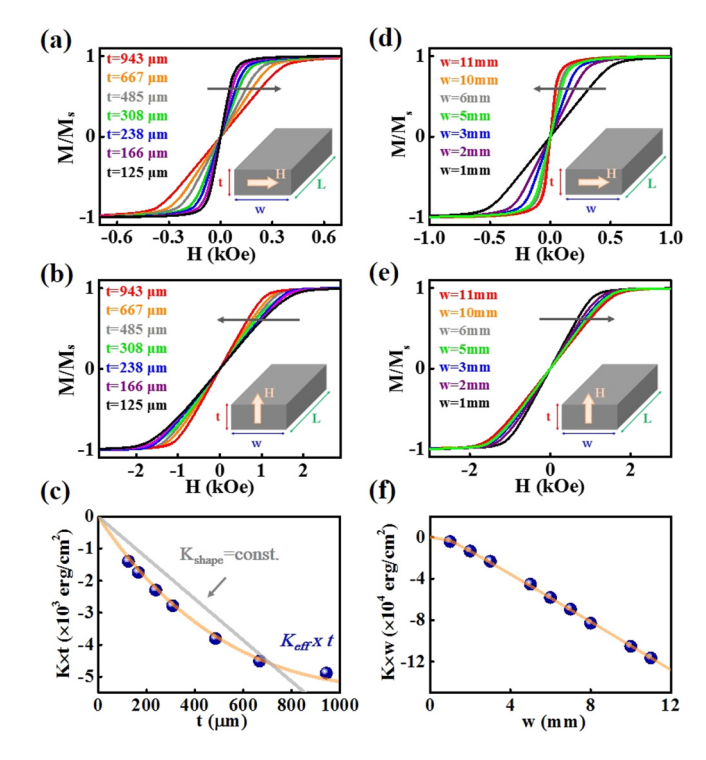


FIG. 3. Normalized M-H loops for YIG with different thicknesses under (a) in-plane  $H_{\parallel}$  and (b) out-of-plane  $H_{\perp}$ . (c) Thickness dependence of total effective anisotropy energy per unit area  $K_{\rm eff}t$  (blue). Orange line is the fitted curve of the thickness dependent  $K_{\rm h}$  of Eq. (4) and the grey line is fitted by a constant  $K_{\rm h}$ . Normalized M-H loops for YIG with different widths under (d) in-plane  $H_{\parallel}$  and (e) out-of-plane  $H_{\perp}$ . (f) Width dependence of total effective anisotropy energy per unit area  $K_{\rm eff}w$  (blue). Orange line is the fitted curve by the width dependent  $K_{\rm h}$  of Eq. (5).

and w, l, and t are chosen along the rectangle principal axes. However, in general, the demagnetizing factor can only be analytically calculated for ellipsoids with a uniform magnetic field [24,25] or evaluated for nonellipsoids with high and low susceptibility limits [26–29]. To quantitatively estimate the effective demagnetizing factor in the ferrimagnetic YIG slab with a nonellipsoidal shape, a small net magnetization, and low susceptibility, we adapted the recent model proposed by Prozorov  $et\ al.$  [30], in which this shape restriction is overcome by a three-dimensional solution of the Maxwell equation with an adaptive mesh for a particular shape. As a result, we can estimate the effective demagnetizing factor for a slab of dimensions w, l, and t as  $N_w^{-1} = 1 + \frac{3}{4} \frac{w}{t} (1 + \frac{t}{L})$  and  $N_t^{-1} = 1 + \frac{3}{4} \frac{w}{w} (1 + \frac{t}{L})$ . Then, the total effective anisotropy energy per unit area can be calculated as follows:

$$(K_{\text{eff}})t = \left[2\pi M^2 \times \left(\frac{1}{1 + \frac{3}{4}\frac{w}{t}(1 + \frac{t}{t})} - \frac{1}{1 + \frac{3}{4}\frac{t}{w}(1 + \frac{w}{t})}\right) + K_{\text{cry}}\right]t. \tag{4}$$

In contrast to the constant  $K_h = -2\pi M^2$  for thin films, as depicted by the grey line in Fig. 3(c), our experimental results can be represented by the shape-dependent  $K_h$  calculated using Eq. (4). The only fitting parameter  $M = 138 \,\mathrm{emu/cm^3}$  is consistent with the bulk value and M-H loop measurement, with the best fit obtained between theory and experimental data, as shown by the orange line in Fig. 3(c).

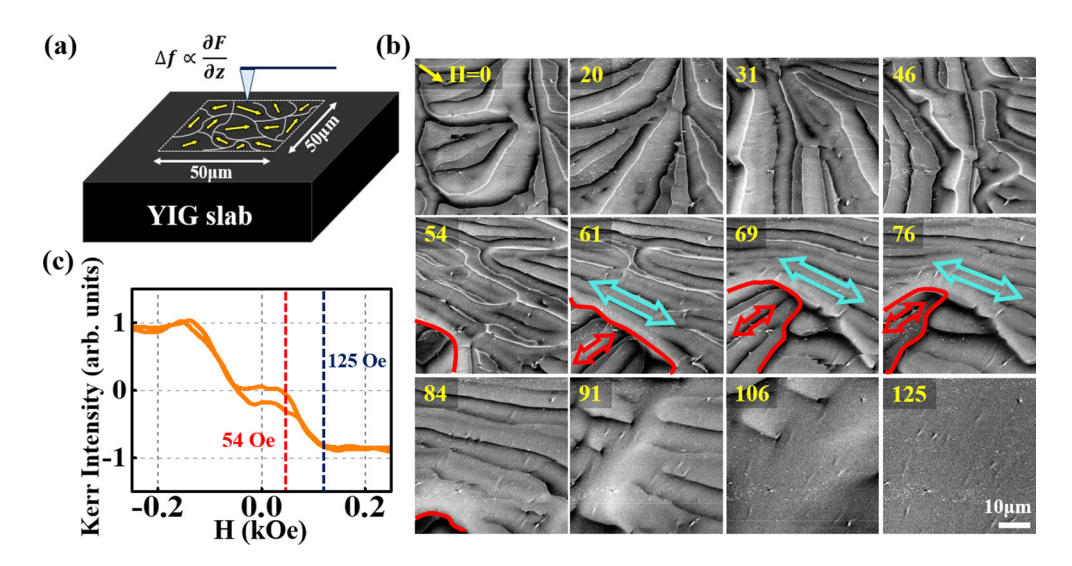


FIG. 4. (a) Schematic diagram for MFM measurement on YIG. (b) Magnetic field dependence of the magnetic domain structure on YIG (287 $\mu$ m) taken in the same  $50 \times 50 \,\mu\text{m}^2$  field of view. Cyan arrow represents the in-plane component of the magnetization in a stripe domain. Red arrow and the enclosed line indicate the general orientation and the region that rotates normal to the external field. Yellow arrow at the top left corner indicates the direction of external in-plane magnetic field with the unit of Oe. The full grey scale of MFM signal in all images is 1.5 Hz. (c) Normalized Kerr intensity with magnetic field along the in-plane magnetic field.

In the case of the width-dependent sample, the in-plane saturation field decreases, whereas the out-of-plane saturation field increases even when the YIG width exceeds 10 mm, as shown in Figs. 3(d) and 3(e), respectively. To analyze the width-dependent sample, the effective demagnetizing factors in Eq. (4) can be modified as

$$(K_{\text{eff}})w = \left[2\pi M^2 \times \left(\frac{1}{1 + \frac{3}{4}\frac{w}{t}(1 + \frac{t}{L})} - \frac{1}{1 + \frac{3}{4}\frac{t}{w}(1 + \frac{w}{L})}\right) + K_{\text{cry}}\right]w.$$
 (5)

As shown in Fig. 3(f), the shape-dependent effective demagnetizing factor in Eq. (5), instead of the constant  $K_h = -2\pi M^2$  for thin films, can accurately describe the width dependence of  $(K_{\rm eff})w$ , with the only fitting parameter  $M=144~\rm emu/cm^3$ . We thus experimentally demonstrated that the numerical model introduced by Prozorov *et al.* is reasonably accurate to account for the demagnetizing factors of a finite slab. Notably, the susceptibility dependence of the demagnetizing factor due to opposite magnetization at two sublattices and the small aspect ratio of the YIG slabs in our work is negligible [28].

To obtain direct insights into the surface magnetic structure and to understand its evolution during the magnetic field sweep, we conducted field-dependent MFM measurements on the YIG single crystals with various thicknesses by using a homemade variable-temperature scanning probe microscope at room temperature in vacuum conditions (see Appendix A for further details). Figure 4(b) shows the MFM images of a 287-µm-thick YIG single crystal under various in-plane fields. We observed randomly oriented magnetic domains with a size of tens of micrometers at H = 0. From H = 0 to 46 Oe, the few domains gradually merge into long stripes, whereas overall, the domains remain similar in size and rotate slowly with the field, corresponding to the plateau in the SSE, SMR, and MOKE measurements. Above 84 Oe, the stripe-shaped domains merge further and increase in size with magnetic vortices formed at the end of the domain walls. When H exceeds the saturation field of 125 Oe, only a single domain, aligned along the external field, remains in the field of view. However, unexpectedly, in the intermediate field region (54 Oe  $\leq H \leq$ 84 Oe), multiple magnetic domains (red enclosed area) can be observed to rapidly rotate nearly 90° toward both their original orientation and the magnetic field, as indicated by the red arrow. Moreover, these domains become larger and then smaller before they eventually align with other stripe domains and the external field. These intriguing domain evolutions revealed by MFM measurements are reproducible. Moreover, they exist only at the YIG surface and are absent in the bulk M-H loop. The magnetic-field-induced 90° flop can be also observed in other YIG single crystals with various thicknesses, such as the 943- $\mu$ m sample, as shown in Fig. 8 in Appendix A. Notably, to impede domain expansion and coherent rotation, the YIG surface must possess magnetic anisotropy that provides an energy barrier to 90° flop rotation of the magnetization. The resulting energy barrier given by  $U_m = MH_{\text{eff}}$  can be overcome by an external effective field  $H_{\text{eff}}$ , where the value can be readily obtained from field-dependent MFM or the half width of the plateau in the SSE, MR, and MOKE measurements. As shown in Fig. 5(a), the obtained  $U_m$  decreases with decreasing thickness and is comparable across independent measurements, whereas it increases with the decreasing width of the YIG, as shown in Fig. 5(b). Such magnetic anisotropy can be attributed to the shape anisotropy and the magnetostatic energy associated with the surface magnetic poles. We further calculated the effective demagnetizing factors by using  $N^*$  (=  $N_w - N_t$ ) for YIG slabs with various thicknesses and

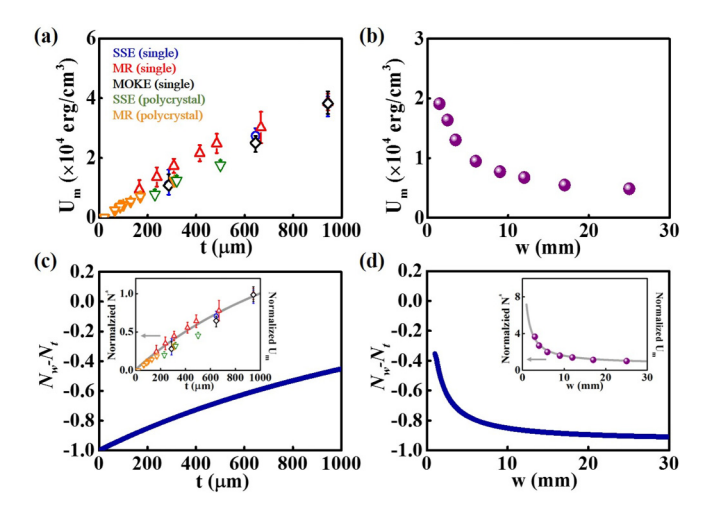


FIG. 5. (a) The thickness and (b) width dependent magnetic potential energy  $(U_{\rm m})$  at YIG surface. (c) The thickness dependent and (d) width dependent demagnetizing factors  $N^* (= N_w - N_t)$ . Inset in (c) and (d) depicts the comparison between the normalized  $U_{\rm m}$  and  $N^*$ .

widths for comparison. Figures 5(c) and 5(d) display similar trends, and the demagnetizing factors accurately represent the experiment results when each value is normalized to unity, as shown in the insets of Figs. 5(c) and 5(d). Consequently, the variable width of the plateau can manifest itself as a different shape of YIG slab.

The PHE measurement further revealed the impact of the  $90^{\circ}$  magnetic rotation on the spin current transport. As shown in Fig. 6, the angular dependence of PHE in Pt (5 nm)/YIG (0.5 mm) under various in-plane magnetic fields exhibits the  $\sin 2\theta$  behavior. However, a clear  $90^{\circ}$  phase shift occurs at a field of 60 Oe. When the magnetic field is larger than the saturation field, surface moments follow the field direction. By contrast, at the onset of the magnetic  $90^{\circ}$  flop transition, surface moments are tilted nearly  $90^{\circ}$  toward the external field, resulting in a sign change in  $\Delta R_{\rm XY}$ , as in the case of the 60-Oe field. This result clearly indicates that the PHE

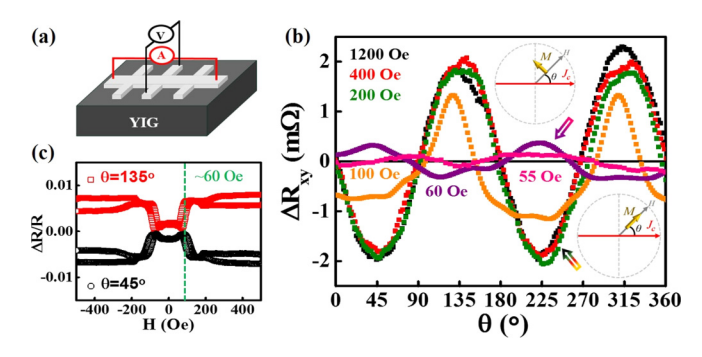


FIG. 6. (a) Schematic diagram for the planar Hall effect (PHE) measurement of Pt(5 nm)/YIG with 10- $\mu$ m-wide Hall bar pattern. (b) The angular dependence of relative PHE resistance  $\Delta R_{\rm XY}$  under different in-plane magnetic field. Insets are schematic drawings of the magnetic moment under 55–60 Oe (upper drawing) or above 200 Oe (lower drawing) at field angle of 225°. (c) Field dependent  $\Delta R_{\rm XY}$  with field angle along 45° (black) and 135° (red).

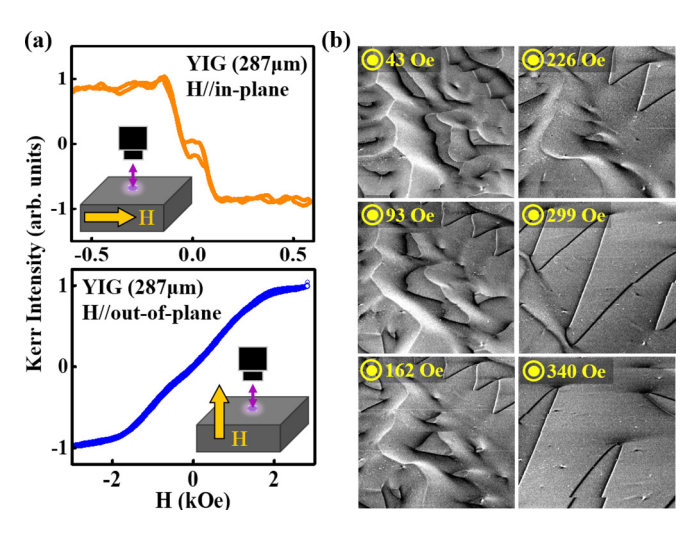


FIG. 7. (a) Normalized Kerr intensity with magnetic field along the in-plane (top) and out-of-plane (bottom) of YIG (287  $\mu$ m). (b) Out-of-plane magnetic field dependence of the magnetic domains on YIG measured by MFM in the same field of view as that in Fig. 4(b).

resistance, being sensitive to surface magnetization switching, can readily capture the 90° rotation of magnetization during the transition of two states in Pt/YIG. By contrast, the 90° resistance phase shift is absent in a general ferromagnetic film, such as Py (see Appendix B and Fig. 9).

When similar measurements are made of the same sample under out-of-plane magnetic fields, magnetic moments are only gradually aligned along the field, and the plateau disappears. As shown in Fig. 7(a), no trace of the plateau is observable when using polar MOKE measurement. In addition, as revealed directly by the MFM images, the magnetic domains expand continuously with the increasing out-of-plane magnetic field displayed in Fig. 7(b), with no indication of the 90° domain flip. This scenario is similar to the spin-flop transition in an antiferromagnet or a ferrimagnet, where the spin-flop transition can only occur if a sufficiently large external magnetic field is applied along the magnetic easy axis, but not along the magnetic hard axis.

#### IV. CONCLUSION

We investigated the effect of the demagnetizing field on the spin transport of Pt/YIG. The demagnetizing factors play a vital role in the thickness and width dependence of transport behaviors, with an anomalous plateau associated with the spin current phenomenon as seen from various independent measurements, including the SSE, SMR, PHE, and MOKE. We demonstrated that the plateau phenomenon is dominated by the effective demagnetization around YIG due to its rather low magnetic anisotropy. The surface of YIG possesses a magnetic energy barrier to the 90° magnetic rotation, as imaged using MFM and verified by the 90° resistance phase shift in angular-dependent PHE. Therefore, the characteristics of spin current not only are sensitive to the surface magnetic property but also reflect the demagnetizing field of the specimen.

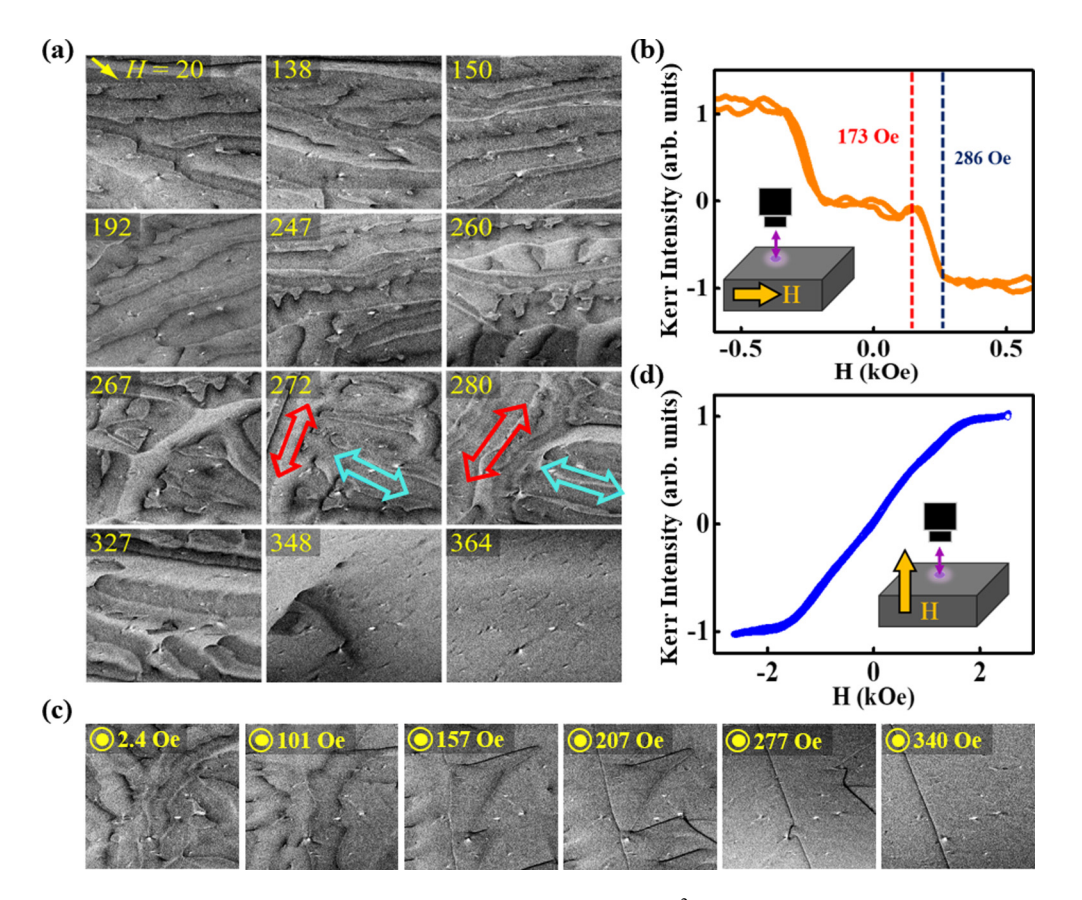


FIG. 8. The magnetic domain on YIG (943  $\mu$ m) in a field of view of  $32 \times 32 \,\mu$ m<sup>2</sup> measured by MFM under (a) in-plane (the direction is indicated by the yellow arrow and the strength in Oe at the top left corner) and (c) out-of-plane magnetic field. The full gray scale of MFM signal is 1.8 Hz in all images. Normalized Kerr intensity with (b) in-plane (d) out-of-plane magnetic field.

#### **ACKNOWLEDGMENTS**

This work was supported by grants from the Ministry of Science and Technology of Taiwan (Grants No. MOST 106-2628-M-002-015-MY3 and No. MOST 109-2123-M-002-002) and partially supported by a grant from Academia Sinica and National Taiwan University (Grant No. AS-NTU-108-09). Work at JHU was supported by NSF DMREF-1729555. T.-M.C. and S.-Y.H. are grateful for the support of a Golden Jade fellowship from Kenda Foundation.

# APPENDIX A: MFM AND MOKE MEASUREMENT ON YIG (943 $\mu m$ )

For magnetic force microscopy (MFM) measurements, we used a homemade variable-temperature scanning probe microscope (from 4.2 K to room temperature) with a fiber-optic interferometer for sensing the cantilever deflection. All MFM measurements were conducted at room temperature and under a vacuum condition of approximately 1 mbar to enhance the MFM sensitivity ( $Q = \sim 400$ ). We used the frequency-modulated tapping mode to obtain the topographic line profile during the first pass, and thereafter, following the same topographic profile with a lift height of 45 nm, the frequency shift of the cantilever was recorded as magnetic signals during the second pass. We used MFM tips with a low moment (NANOSENSORS PPP-LM-MFMR) to minimize the effect

from the tip stray field. The tips were magnetized perpendicular to the sample surface by using a strong permanent magnet before each measurement.

The evolution of the magnetic domain during magnetic state transition can be observed on the surface of YIG with various thicknesses. As shown in Fig. 8(a), the magnetic domains and domain walls under different in-plane magnetic fields on YIG with a thickness of 943  $\mu$ m are clearly visible through MFM. When the magnetic field is increased to 364 Oe, a single magnetic domain forms the full field of view. When the magnetic field is low, less than approximately 170 Oe, as shown by the plateau regime from MOKE measurement in Fig. 8(b), the magnetic multidomain remains essentially similar. Crucially, in the intermediate field regime,

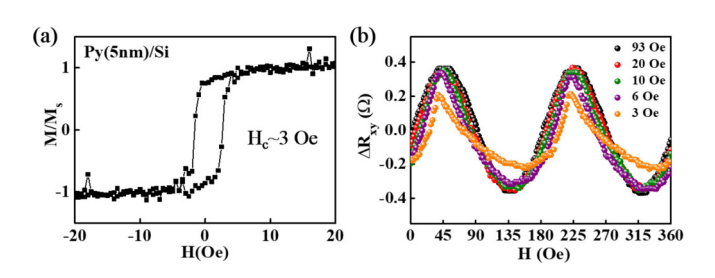


FIG. 9. (a) The field dependent magnetization and (b) the angle dependent PHE signal for Py(5 nm)/Si.

below the saturation and above the plateau field, a sudden rotation of the magnetic domain to nearly  $90^{\circ}$  relative to the magnetic field direction can be observed. Here, based on the MOKE results, the width of the plateau on the 943- $\mu$ m-thick YIG is larger than that on the 287- $\mu$ m-thick YIG, indicating that the surface magnetic potential energy on the YIG is thickness dependent. However, if the magnetic field is applied along the out-of-plane direction, the hard axis, the magnetic domains only expand with increasing magnetic field, without a  $90^{\circ}$  domain flip, as shown in Fig. 8(c). This finding is consistent with the MOKE signal in the out-of-plane magnetic field, where no trace of plateau behavior is observed [Fig. 8(d)].

## APPENDIX B: ANGULAR-DEPENDENT PLANAR HALL EFFECT IN Py

For comparison, we also measured the angular-dependent planar Hall effect (PHE) in a conventional ferromagnet, Py. As shown in Fig. 9, the amplitude of the planar Hall signal decreases monotonically with the decreasing magnetic field. Most critically, unlike the case in Pt/YIG, the 90° phase shift is absent, despite the larger magnetization (eight times larger than YIG) of Py and stronger dipolar interaction. Therefore, the intrinsic magnetic state transition, instead of unintentionally induced domain rotation caused by the dipolar field, magnetic field, current, or any other artifact, is observed in Pt/YIG.

- J. Sinova, S. O. Valenzuela, J. Wunderlich, C. H. Back, and T. Jungwirth, Rev. Mod. Phys. 87, 1213 (2015).
- [2] Y. Kajiwara, K. Harii, S. Takahashi, J. Ohe, K. Uchida, M. Mizuguchi, H. Umezawa, H. Kawai, K. Ando, K. Takanashi, S. Maekawa, and E. Saitoh, Nature (London) 464, 262 (2010).
- [3] Y. S. Chen, J. G. Lin, S. Y. Huang, and C. L. Chien, Phys. Rev. B 99, 220402(R) (2019).
- [4] S. Y. Huang, X. Fan, D. Qu, Y. P. Chen, W. G. Wang, J. Wu, T. Y. Chen, J. Q. Xiao, and C. L. Chien, Phys. Rev. Lett. 109, 107204 (2012).
- [5] K.-i. Uchida, J.-i. Ohe, T. Kikkawa, S. Daimon, D. Hou, Z. Qiu, and E. Saitoh, Phys. Rev. B 92, 014415 (2015).
- [6] R. Lebrun, A. Ross, O. Gomonay, S. A. Bender, L. Baldrati, F. Kronast, A. Qaiumzadeh, J. Sinova, A. Brataas, R. A. Duine, and M. Kläui, Commun. Phys. 2, 50 (2019).
- [7] R. Lebrun, A. Ross, S. A. Bender, A. Qaiumzadeh, L. Baldrati, J. Cramer, A. Brataas, R. A. Duine, and M. Kläui, Nature (London) 561, 222 (2018).
- [8] K. Uchida, H. Adachi, T. Ota, H. Nakayama, S. Maekawa, and E. Saitoh, Appl. Phys. Lett. 97, 172505 (2010).
- [9] D. Qu, S. Y. Huang, J. Hu, R. Wu, and C. L. Chien, Phys. Rev. Lett. 110, 067206 (2013).
- [10] T. Kikkawa, K. Uchida, Y. Shiomi, Z. Qiu, D. Hou, D. Tian, H. Nakayama, X.-F. Jin, and E. Saitoh, Phys. Rev. Lett. 110, 067207 (2013).
- [11] S. Seki, T. Ideue, M. Kubota, Y. Kozuka, R. Takagi, M. Nakamura, Y. Kaneko, M. Kawasaki, and Y. Tokura, Phys. Rev. Lett. 115, 266601 (2015).
- [12] J. Li, C. B. Wilson, R. Cheng, M. Lohmann, M. Kavand, W. Yuan, M. Aldosary, N. Agladze, P. Wei, M. S. Sherwin, and J. Shi, Nature (London) 578, 70 (2020).
- [13] P. Vaidya, S. A. Morley, J. van Tol, Y. Liu, R. Cheng, A. Brataas, D. Lederman, and E. D. Barco, Science 368, 160 (2020).

- [14] G. E. W. Bauer, E. Saitoh, and B. J. van Wees, Nat. Mater. 11, 391 (2012).
- [15] A. Hoffmann and S. D. Bader, Phys. Rev. Appl. 4, 047001 (2015).
- [16] K. Uchida, H. Adachi, T. Kikkawa, A. Kirihara, M. Ishida, S. Yorozu, S. Maekawa, and E. Saitoh, Proc. IEEE 104, 1946 (2016).
- [17] Y.-J. Chen and S.-Y. Huang, Phys. Rev. Lett. **117**, 247201 (2016).
- [18] F.-J. Chang, J. G. Lin, and S.-Y. Huang, Phys. Rev. Mater. 1, 031401(R) (2017).
- [19] P.-H. Wu and S.-Y. Huang, Phys. Rev. B **94**, 024405 (2016).
- [20] M. T. Johnson, P. J. H. Bloemen, F. J. A. D. Broeder, and J. J. D. Vries, Rep. Prog. Phys. 59, 1409 (1996).
- [21] P. G. Gowtham, G. M. Stiehl, D. C. Ralph, and R. A. Buhrman, Phys. Rev. B **93**, 024404 (2016).
- [22] J. Fu, M. Hua, X. Wen, M. Xue, S. Ding, M. Wang, P. Yu, S. Liu, J. Han, C. Wang, H. Du, Y. Yang, and J. Yang, Appl. Phys. Lett. 110, 202403 (2017).
- [23] W. H. Von Aulock, *Handbook of Microwave Ferrite Materials* (Academic, London, 1965).
- [24] E. C. Stoner, Philos. Mag. 36, 803 (1945).
- [25] J. A. Osborn, Phys. Rev. 67, 351 (1945).
- [26] R. I. Joseph and E. Schlömann, J. Appl. Phys. **36**, 1579 (1965).
- [27] R. I. Joseph, J. Appl. Phys. 38, 2405 (1967).
- [28] D.-X. Chen, E. Pardo, and A. Sanchez, IEEE Trans. Magn. 38, 1742 (2002).
- [29] D.-X. Chen, E. Pardo, and A. Sanchez, IEEE Trans. Magn. 41, 2077 (2005).
- [30] R. Prozorov and V. G. Kogan, Phys. Rev. Appl. 10, 014030 (2018).